Ab initio optical calculation by RESPACK

Kazuma NAKAMURA
Graduate School of Engineering, Kyushu Institute of Technology
1-1 Sensui-cho, Tobata, Kitakyushu, Fukuoka, 804-8550

1 Introduction

In this report, we present optical-response calculations of materials using first-principles calculation software RESPACK [1]. *Ab initio* optical-response calculations have been performed for a long time, and have contributed to the understanding of materials through quantitative comparisons between theoretical and experimental spectra. However, since the calculation is heavier than normal band calculations, it was often performed for small systems containing a small number of atoms. In recent years, with advances in computers and the spread of open software, the calculation has become possible even for large systems. RESPACK is one of such software and is increasingly being used to understand the optical response of complex and large systems. In this report, we would like to introduce some recent results of the optical response calculations using RESPACK.

2 Method

In this section, we briefly describe a calculation detail. The symmetric dielectric function [2] can be written with using the polarization function as

$$\begin{aligned}&\epsilon_{\mathbf{GG}'}(\mathbf{q},\omega)\\ =\ &\delta_{\mathbf{GG}'}-\frac{4\pi}{\Omega}\frac{1}{|\mathbf{q}+\mathbf{G}|}\chi_{\mathbf{GG}'}(\mathbf{q},\omega)\frac{1}{|\mathbf{q}+\mathbf{G}'|},\end{aligned} \tag{1}$$

where $\chi_{\mathbf{GG}'}(\mathbf{q},\omega)$ is the Fourier transform of the polarization function, and the explicit expression can be found in Ref. [1]. $\mathbf{q}$ and ω are wavevector in the Brillouin zone and frequency, respectively, and $\mathbf{G}$ is reciprocal vector. Ω is the volume of the unit cell.

The optical response is related to $\mathbf{q}\sim\mathbf{0}$, and in the calculation of $\epsilon_{\mathbf{GG}'}(\mathbf{q},\omega)$, the head component which corresponds to the $\mathbf{G}=\mathbf{G}'=\mathbf{0}$ component in the $\mathbf{q}\to\mathbf{0}$ limit must be treated carefully. For the head component, we calculate the following [3]

$$\lim_{\mathbf{q}\to\mathbf{0}}\epsilon_{\mathbf{00}}(\mathbf{q},\omega)=1-\frac{4\pi}{\Omega}\frac{\partial^2\chi_{\mathbf{00}}(\mathbf{q},\omega)}{\partial q^2}-\frac{(\omega_{pl}^{\mu\nu})^2}{\omega(\omega+i\delta)}. \tag{2}$$

Here, the last term results from the intraband transition, and δ is a smearing factor. ω_{pl} is the bare plasma frequency calculated via the Fermi-surface integral as

$$\omega_{pl}^{\mu\nu}=\frac{1}{N_k}\sum_{\mathbf{k}}^{N_k}\sum_{\alpha}p_{\alpha\alpha\mathbf{k}}^{\mu}p_{\alpha\alpha\mathbf{k}}^{\nu}\delta(E_{\alpha\mathbf{k}}-E_F), \tag{3}$$

where E_F is the Fermi energy determined in the density functional band calculation, and $p_{\alpha\alpha\mathbf{k}}^{\nu}$ is the diagonal element of the transition-moment matrix with respect to the bands as

$$\begin{aligned}p_{\alpha\beta\mathbf{k}}^{\mu}&=-i\Big\langle\psi_{\alpha\mathbf{k}}\Big|\frac{\partial}{\partial x_\mu}+[V_{NL},x_\mu]\Big|\psi_{\beta\mathbf{k}}\Big\rangle\\ &\sim-i\Big\langle\psi_{\alpha\mathbf{k}}\Big|\frac{\partial}{\partial x_\mu}\Big|\psi_{\beta\mathbf{k}}\Big\rangle\end{aligned} \tag{4}$$

with x_μ being the Cartesian coordinate. On the above evaluation, we ignore the contribution from the non-local part of the pseudopotential, V_{NL}. We note that, in the optical response, the non-local pseudopotential contribution may sometimes manifest itself as a significant effect, especially for the transition metals [4].

The optical properties such as the macroscopic dielectric function $\epsilon_{\mathrm{M}}(\omega)$, the real part of the optical conductivity $\sigma(\omega)$, and the reflectance spectrum $R(\omega)$ are calculated from the inverse of the matrix $\epsilon_{\mathbf{GG}'}(\mathbf{q},\omega)$ in Eqs.(1) and (2) as

$$\epsilon_{\mathrm{M}}(\omega)=\lim_{\mathbf{q}\to0}\frac{1}{\epsilon^{-1}_{\mathbf{00}}(\mathbf{q},\omega)}, \tag{5}$$

$$\mathrm{Re}\big[\sigma(\omega)\big]=\frac{\omega}{4\pi}\mathrm{Im}\lim_{\mathbf{q}\to0}\frac{1}{\epsilon^{-1}_{\mathbf{00}}(\mathbf{q},\omega)}, \tag{6}$$

and

$$R(\omega)=\left|\frac{1-\sqrt{\lim_{\mathbf{q}\to0}\epsilon^{-1}_{\mathbf{00}}(\mathbf{q},\omega)}}{1+\sqrt{\lim_{\mathbf{q}\to0}\epsilon^{-1}_{\mathbf{00}}(\mathbf{q},\omega)}}\right|, \tag{7}$$

respectively.

3 Results and Discussions

Below, we show some applications of RESPACK. We performed *ab initio* density function calculations using Quantum Espresso [5, 6] in which the wave functions were expanded on a plane-wave basis. We employed norm-conserving pseudopotentials, and the generalized-gradient approximation for the exchange-correlation energy. The cutoff energies for the wave function and charge density are 100 Ry and 400 Ry, respectively. The calculation condition of the optical calculations is as follows: The energy cutoff for the polarization function was set to 10 Ry. The total number of bands considered in the polarization calculation was determined to cover unoccupied states up to 10-15 eV above E_F. The details of the k-point sampling vary depending on the system, so we will describe it in each section of materials.

3.1 WC

The first example is tungsten carbide WC. Recently, we found that the WC can be a good candidate for solar selective absorber [7]. Sunlight absorption and its efficient use of energy is an important topic and is being actively studied worldwide. The sunlight energy range is from 0.5 to 4.1 eV, and the important problem is to find materials that can selectively absorb light in this energy range. As a basis for the material design, we focus on plasma excitations, especially in a low energy [8]. The plasma excitation is the collective excitation of electrons in metals, and some materials have the plasma excitation with an excitation energy of 0.1-1.0 eV around the cutoff of the sunlight energy. The WC is one of the main components in a TiCN-based cermet widely used as a cutting tool. Through the *ab initio* electronic-structure analysis for the wasted TiCN-based cermet, we found that the WC has a low-energy plasma excitation of 0.6 eV exactly corresponding to the sunlight cutoff [7].

Figure 1(a) is our calculated band structures (red solid curves) of the WC being a hexagonal closed pack (hcp) structure and containing 2 atoms in the unit cell. The k-point sampling is $32 \times 32 \times 32$. A spin-orbit interaction (SOI) of tungsten is known to be nearly 0.4 eV, then we calculated the SOI band structure and compared it with that without the SOI (black solid curves). The SOI can bring about a splitting of the low-energy bands, but the effect

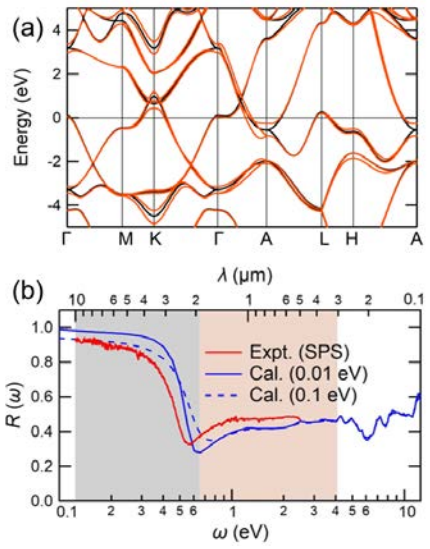

Figure 1: (a) Comparison between *ab initio* density functional band structure of WC with (red solid curves) and without (black solid curves) the SOI. The energy zero is the Fermi level. Dispersions of the WC are plotted along the high symmetry points in the Brillouin zone, where Γ= (0, 0, 0), M = (1/2, 0, 0), K = (1/3, 1/3, 0), A = (0, 0, 1/2), L = (−1/2, 0, 1/2), and H = (1/3, 1/3, 1/2), where the coordinates are represented in terms of basic vectors of the reciprocal lattice of the hcp lattice. (b) Comparison of experimental (red-solid line) and *ab initio* (blue-solid line) reflectance spectra with a smearing of 0.01 eV. We also show an *ab initio* result (blue dashed line) with smearing of 0.1 eV. In the figure, the bright orange shadow represents the spectral range of sunlight, and the gray shadow represents the range of radiation.

is basically small. Figure 1(b) is the comparison of the experimental (red-solid line) and our calculated *ab initio* (blue-solid line) reflectance spectra with a smearing of 0.01 eV. The WC sample was prepared as a polycrystalline obtained with the spark plasma sintering (SPS) method. The spectrum with the SOI was calculated with the spinor version of RESPACK [9]. We see a clear plasma edge around 0.6 eV (2.0 μm) corresponding to the cutoff energy of the sunlight spectrum. Around the low-energy (0.1-0.5 eV), we see the lowering of the experimental reflectance compared with the theoretical spectrum, which would be due to the multiple scattering in the pores on the polycrystalline WC surface. To consider this point, we calculated an *ab initio* reflection spectra with a smearing factor of 0.1 eV, denoted by the blue-dashed line, where the smearing size qualitatively represents the strength

of scattering by impurities. As can be seen by comparing the result with the smearing factor of 0.01 eV, increasing the smearing broadens the spectrum.

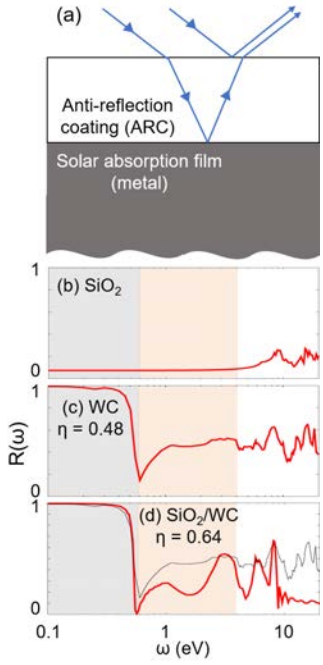

Figure 2: (a) Reflectance property of the WC system including anti-reflection coating (ARC). (b) *Ab initio* reflectance of SiO_2 as ARC and (c) WC as solar absorption film. (d) A film-interference simulation result with the *ab initio* inputs.

We next discuss the discrepancy in the high energy region (0.6-4.0 eV). In this region, the reflectance is large as ~ 0.5, which must be reduced for the preferable solar absorption. The figure of merit η for the solar absorption of the bulk WC was estimated as 0.48 [7], which is not so high and the origin is the high reflectance in the region of 0.6-4.0 eV. In this case, anti-reflection coating (ARC) is effective to suppress the higher-energy reflectance [Fig. 2(a)]. To evaluate the suppression effect by the ARC, we perform a film-interference simulation with insulator SiO_2 for the ARC.

The calculation proceeds as follows: We first consider a reflection coefficient of Air and ARC as

$$r_{\mathrm{Air-ARC}}(\lambda) = \frac{N_{\mathrm{Air}} - N_{\mathrm{ARC}}(\lambda)}{N_{\mathrm{Air}} + N_{\mathrm{ARC}}(\lambda)}, \tag{8}$$

where N_{Air} and $N_{\mathrm{ARC}}(\lambda)$ are reflective index of Air and ARC, respectively. The λ is the wavelength of light. Similarly, a reflection coefficient of WC and ARC is given as

$$r_{\mathrm{ARC-WC}}(\lambda) = \frac{N_{\mathrm{ARC}}(\lambda) - N_{\mathrm{WC}}(\lambda)}{N_{\mathrm{ARC}}(\lambda) + N_{\mathrm{WC}}(\lambda)} \tag{9}$$

with $N_{\mathrm{WC}}(\lambda)$ being a reflective index of the WC. By using these quantities, the reflectance spectrum of the total system is calculated as

$$R(\lambda) = \frac{r_{\mathrm{Air-ARC}}(\lambda) + r_{\mathrm{ARC-WC}}(\lambda)e^{i\Delta(\lambda)}}{1 + r_{\mathrm{Air-ARC}}(\lambda)r_{\mathrm{ARC-WC}}(\lambda)e^{i\Delta(\lambda)}} \tag{10}$$

with

$$\Delta(\lambda) = \frac{4\pi d_{\mathrm{ARC}} N_{\mathrm{ARC}}(\lambda)}{\lambda}. \tag{11}$$

Here d_{ARC} is a thickness of ARC. We note that all the parameters can be calculated from first-principles.

Figure 2 summarizes the results about the WC system. The panels (b) and (c) display *ab initio* reflectance spectra of the bulk SiO_2 as an ARC and WC as a solar absorber, respectively. With these *ab initio* data , the reflectance spectrum of the total ARC/WC system is obtained in Fig. 2(d), where we found a significant improvement of η from 0.48 to 0.64.

3.2 Interface system

The second example is the transition-metal oxide $SrVO_3$ (SVO). SVO is a famous strongly correlated metal and an important benchmark in studying electronic correlations in materials. We found that the SVO also exhibits the low-energy plasma excitation of 1.6 eV [8] somewhat higher than the solar absorption range. We found that, based on *ab initio* calculations, by depositing SVO films on $SrTiO_3$ (STO) substrate, the plasma excitation energy can be reduced from 1.6 to 0.7 eV. Thus, the STO/SVO system is a fascinating system as the solar absorbing device. Here, we show the electronic structure and reflectance spectrum of the interface system of the STO/SVO hetero structure.

Figure 3 shows our structure models to be analyzed, where we consider a multilayer model consisting of SVO and STO blocks [panel (a)] and a symmetric slab model [(b)]. The slab model includes a vacuum region with 20 Å, and has a mirror symmetry with respect to the central TiO_2 plane. Then, artificial electric fields due to asymmetry in the both ends of the slab do not occur. The structural models include several SVO blocks, where we specify the number of the blocks as n. In the

present study, we consider the structural models until $n = 4$. The number of the STO blocks was fixed to 5 for the multilayer and 8.5 for the slab (0.5 indicates an additional central TiO_2 layer).

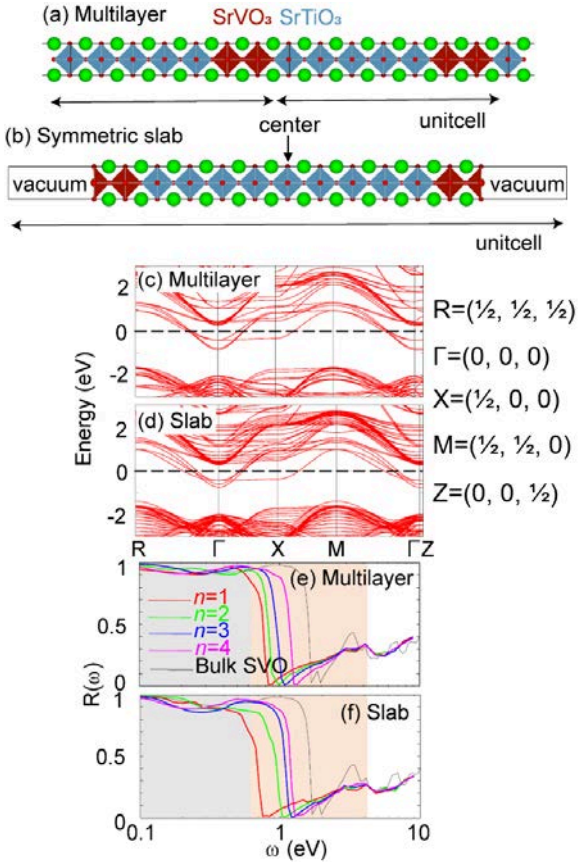

Figure 3: Two structural model: (a) Multilayer consisting of $SrTiO_3$ and $SrVO_3$ blocks. (b) Symmetric slab having a mirror symmetry with respect to the center TiO_2 plane. Our calculated band structures of (c) multilayer and (d) slab model where we show the $n = 2$ case. Panels (e) and (f) show our calculated reflectance spectra of multilayer and slab models, respectively.

Figure 3 shows our calculated band structures of the multilayer (c) and slab (d) with the $k = 10 \times 10 \times 2$ sampling, where the band structures for the $n = 2$ model are displayed. From the band structures, we see that both two systems are metal; the SVO t_{2g} bands cross E_F, and the STO t_{2g} band is about 1 eV above from E_F. Figures 3(e) and (f) show our calculated reflectance spectra for the multilayer and slab models, respectively. We see that the both spectra exhibit a lowering of the plasma edge compared to the bulk SVO one. We also see the appreciable n dependence of the plasma edge; by reducing the SVO thickness, the plasma edge becomes lower. The difference between the multilayer and slab results seems to be small. We estimate the $n = 1$ slab gives $\eta = 0.73$ clearly improving the bulk SVO of $\eta = 0.46$.

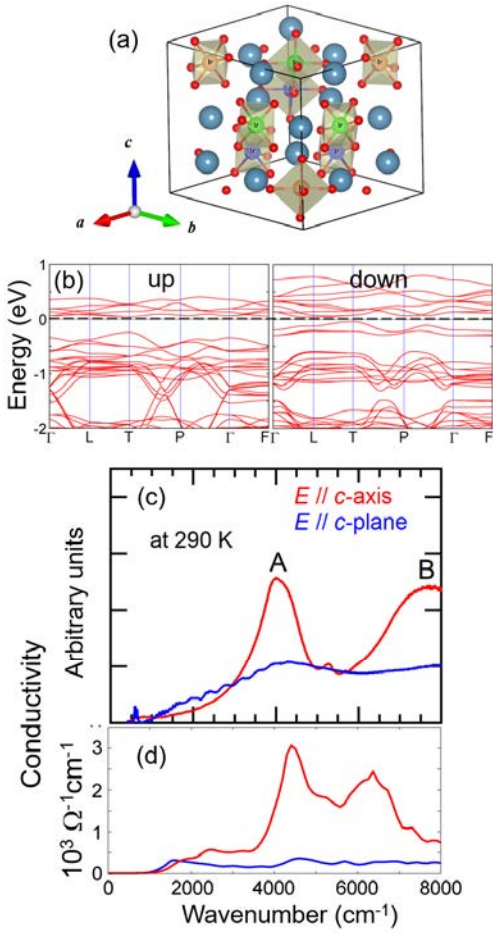

Figure 4: (a) Crystal structure of $\sqrt{3}a \times \sqrt{3}a \times 3c$ superlattice of $Ca_5Ir_3O_{12}$ (space group: R_3). Red, green, and blue spheres are nonequivalent Ir atoms which are the center of an IrO_6 octahedron. (b) *Ab initio* spin density functional band structure, where Γ= (0, 0, 0), L = (1/2, 0, 0), T = (1/2, −1/2, 1/2), P = (0.24, −0.76, 0.24), and F = (1/2, −1/2, 0), and the coordinates are represented in terms of basic vectors of the reciprocal lattice of trigonal lattice. (c) Experimental optical conductivity with polarization parallel to the c-axis (red line) and the c-plane (blue line) at 290 K. (d) Our calculated *ab initio* optical conductivity.

3.3 $Ca_5Ir_3O_{12}$

The third example is $Ca_5Ir_3O_{12}$. This material undergoes two phase transition at 105 K and 7 K [10], and the mechanisms related to so-called hidden or-

der have been very actively debated recently. Experimentally, this is an insulator from above room temperature [11], but *ab initio* density functional calculations predict a metal. Recently, the optical conductivity was measured, and no Drude-like behavior was observed, indicating that it is also the insulator with the optical probe [12]. Thus, the *ab initio* calculation and the experiments do not match, and the origin of the insulation remains unclear. Inelastic X-ray diffraction experiments have detected the superlattice reflection [13] indicating that the structure after the first transition at 105 K changes a $3a \times 3a \times 3c$ superlattice [Fig. 4(a)], and the space group is R_{3m}. Here, we perform *ab initio* spin density functional calculations for the superlattice and investigate the origin of the insulating gap.

Figure 4(b) is our calculated spin density functional band structure for the superlattice containing 60 atoms with the $k = 4 \times 4 \times 4$ sampling, where we see an insulating gap of near 0.2 eV. Also, Figs. 4(c) and (d) shows a comparison of experimental and theoretical optical conductivity. The red lines are the spectra for light with an electric field parallel to the c-axis, and the blue lines are the spectra for light with an electric field parallel to the c-plane. In the experiment, we see two-peak structure denoted by A and B in the spectrum of $E \parallel c$-axis, which are well reproduced with the *ab initio* calculations.

3.4 Ta_4SiTe_4

The fourth example is Ta_4SiTe_4. Recently, a single crystal of one-dimensional telluride Ta_4SiTe_4 and its Mo-doped samples were reported to exhibit a very large $|S|$ with sufficiently small ρ for thermoelectric materials over wide temperatures from 50 K to room temperature [14]. Ta_4SiTe_4 has a one-dimensional crystal structure with the orthorhombic *Pbam* space group, consisting of Ta_4SiTe_4 chains loosely bounded by van der Waals interactions between Te atoms, in Fig. 5(a). The Ta_4SiTe_4 chains lie parallel to the c-axis, forming an almost perfect triangular lattice in the ab plane, and making the material almost isotropic in this plane. The insulating gap is estimated as 0.1-0.15 eV.

Figure 5(b) is the experimental optical conductivity of Ta_4SiTe_4 at room temperature [15]. Blue and red lines are the optical conductivity for $E \parallel c$ $[\sigma_{\parallel}(\omega)]$ and $E \perp c$ $[\sigma_{\perp}(\omega)]$. $\sigma_{\parallel}(\omega)$ has peaks at 2.5, 1.9, 1.3, and 0.2 eV. The first three peaks in the near-infrared to visible region most likely correspond to the interband transition. The last peak at 0.2 eV corresponds to the band gap at E_F. In contrast, $\sigma_{\perp}(\omega)$ also has a small peak at around 0.2 eV, but does not show a clear peak due to the interband transition. These behaviors are well reproduced by the *ab initio* calculation with the $k = 4 \times 2 \times 9$ sampling, shown in Fig. 5(c). The theoretical spectrum for $E \parallel c$ has four prominent peaks at 2.5, 2.0, 1.4, and 0.4 eV, and the spectra of $E \parallel a$ and $E \parallel b$ are almost identical and have no significant structure other than a strong decrease below 0.2–0.4 eV. These are totally consistent with the experiments.

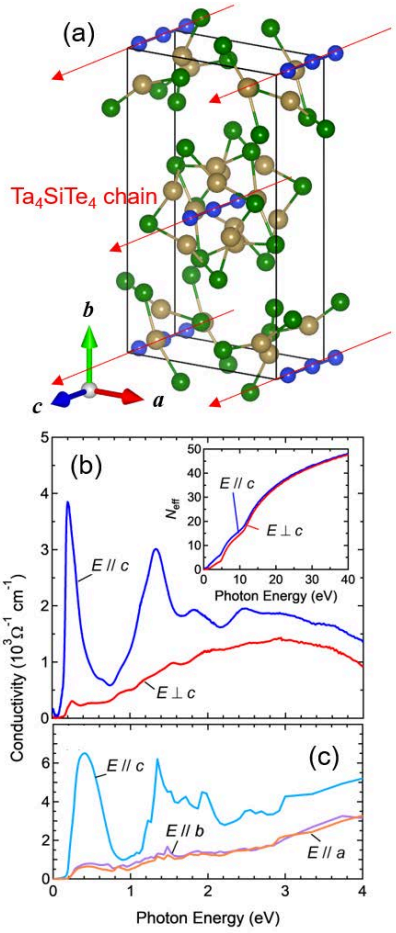

Figure 5: (a) Crystal structure of Ta_4SiTe_4 with orthorhombic unit cell (space group: *Pbam*). Blue, green, and brown spheres are Si, Te, and Ta atoms, respectively. (b) Experimental optical conductivity of a Ta_4SiTe_4 single crystal parallel and perpendicular to the c-axis at room temperature. The inset shows the effective number of electrons per formula unit. (c) *Ab initio* optical conductivity spectra of Ta_4SiTe_4 parallel to the a-, b-, and c-axes.

3.5 Ruby

For remaining parts, we introduce applications of RESPACK other than optical property. The first example is an excitation-energy calculation of the impurity system of ruby (Al_2O_3:Cr). Figure 6(a) is the atomic geometry and the panel (b) is our calculated band structure with the $k = 3 \times 3 \times 3$ sampling, where we see two impurity bands near E_F due to the Cr impurity. Blue dotted lines are the Wannier interpolated band obtained from RESPACK-wannier program. By using RESPACK, we derived an *ab initio* effective low-energy model for the five d orbitals of the Cr impurity.

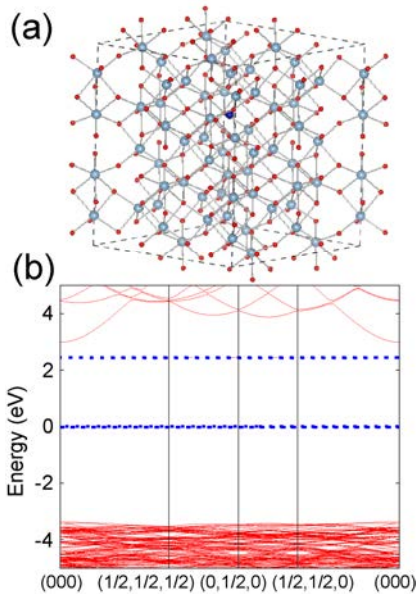

Figure 6: (a) Atomic geometry for impurity system: $Al_{47}CrO_{72}$ (2×2×1 supercell containing 120 atoms). (b) Our calculated band structure with the $k = 3\times3\times3$ sampling using xTAPP [16]. Blue dotted lines represent the Wannier interpolated bands for the impurity levels.

When the RESPACK job is executed, a directory `dir-mvmc` is generated under the calculation directory, and the files necessary for model-analysis softwares mVMC [17] and $\mathcal{H}\Phi$ [18] are output. Using these data and a standard-mode input for mVMC and $\mathcal{H}\Phi$, all inputs of the model calculations are automatically generated under the following command:

```
HPhi -s stan.in (or vmc.out -s stan.in)
```

Here, `HPhi` and `vmc.out` are execution files of $\mathcal{H}\Phi$ and mVMC, respectively, and `stan.in` is an input file for standard mode. This interface code has the lattice conversion function; when the user moves from *ab initio* calculation to model one, the lattice adopted at the *ab initio* calculation can be flexibly changed. Also, the code has an option for avoiding the Hartree-term double count; user can adjust one-body correction $\Delta_{i\mathbf{0}}$ by optional parameter α,

$$\begin{aligned}\Delta_{i\mathbf{0}} &= \alpha U_{i\mathbf{0},i\mathbf{0}} D^{\mathrm{KS}}_{i\mathbf{0},i\mathbf{0}} \\ &+ \sum_{\mathbf{R}\neq\mathbf{0}} \sum_{k} D^{\mathrm{KS}}_{k\mathbf{0},k\mathbf{0}} \Big(U_{i\mathbf{0},k\mathbf{R}} - (1-\alpha) J_{i\mathbf{0},k\mathbf{R}} \Big),\end{aligned} \tag{12}$$

where U, J, and D are the direct integral, exchange integrals, and density matrix with the Kohn-Sham orbital, respectively.

Table 1 shows our calculated excitation energy diagram of the impurity model. The excitation energy depends on α in Eq. (12), and the results correcting of the Hartree-term double counting ($\alpha = 1$) reasonably reproduce the experimental result.

Table 1: Calculated energy diagram of impurity model from RESPACK + $\mathcal{H}\Phi$. The unit is eV. Values of the ground state (GS) are the total energy.

Expt	Theory		
	$\Delta_{i\mathbf{0}} = 0$	$\alpha = 0.5$	$\alpha = 1$
GS(^4A)	47.9(^4A)	5.60(^4A)	−3.04(^4A)
1.79(^2E)	1.67(^2E)	1.61(^2E)	1.62(^2E)
1.87(^2T)	1.78(^2T)	1.73(^2T)	1.84(^2T)
2.23(^4T)	2.29(^4T)	1.79(^4E)	2.32(^2A)
2.62(^2T)	2.46(^4T)	2.23(^4T)	2.56(^4T)
3.10(^4T)	2.69(^2T)	2.60(^4A)	2.78(^4T)

3.6 La_2CuO_4

Next example is La_2CuO_4, where we would like to introduce Wannier function analysis to understand piezosuperconductivity with a bending strain. It is known that a superconducting transition temperature T_c can be changed with pressure and strain. An epitaxial strain is one of well-known mechanisms of changing T_c by strain. In this treatment, however, the T_c is not changed after sample preparation is completed. Recently, Horide et. al. have developed a new-type strain-processing method that can control material properties adiabatically and continuously by bending strain [19].

We have applied the method to superconducting $La_{2-x}Sr_xCuO_4$ (LSCO), where the structure is freely controlled to be compressed or stretched. From the experiment, they found that the compressive strain for LSCO leads to increasing T_c, while the tensile strain brings about decreasing T_c. In the present study, to understand this trend microscopically, we perform electronic-structure analysis for La_2CuO_4 being a mother compound of the LSCO from first principles.

Figures 7(d) and (e) display our calculated Cu-d_{z^2} and Cu-$d_{x^2-y^2}$ Wannier orbitals, respectively. By using these two orbitals, we performed a fat-band analysis for original density functional band structure. These results are summarized in Fig. 7(f). We see that the fat band due to the Cu-$d_{x^2-y^2}$ (blue) is almost constant for all the strained configurations, while that from the Cu-d_{z^2} (green) appreciably increases from compressive-bent to tensile-bent configurations. This trend is well correlated with the experimental T_c trend with bending strain. It is known that the T_c of the cuprate can increase with purification of the Cu-$d_{x^2-y^2}$ orbital in the Fermi surface (FS) [20]. The present result is consistent with this view; the compressive strain brings about suppressing the Cu-d_{z^2} weight in the FS, leading to increasing T_c.

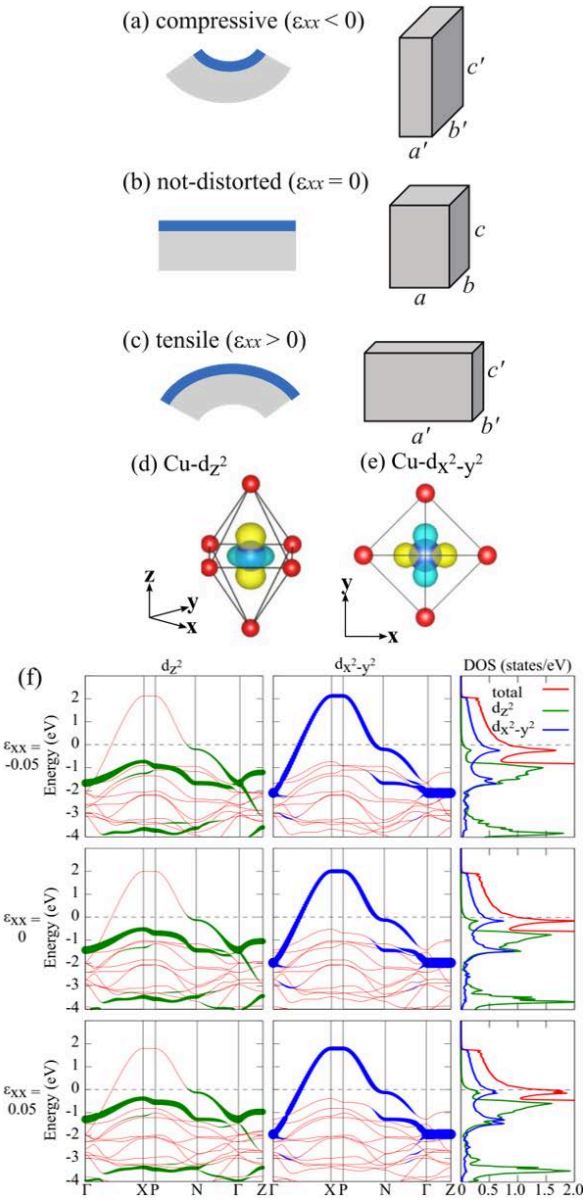

Figure 7: (a)-(c): Schematic figure of strained configurations and corresponding unit cells: (a) compressive-bent, (b) unbent, and (c) tensile-bent structures. Left panels show schematic strained samples, and right panels show deformed unit cells with strain ϵ_{xx}. Maximally localized Wannier orbitals of (d) Cu-d_{z^2} and (e) Cu-$d_{x^2-y^2}$ calculated with RESPACK. (f) Fat-band plots with Cu-d_{z^2} (left) and Cu-$d_{x^2-y^2}$ (center) contributions, and density of states (DOS) (right) for strain $\epsilon_{xx} = -0.05$, 0, and 0.05. Dispersions are plotted along the high symmetry points in the Brillouin zone, where Γ= (0, 0, 0), X = (1/2, 0, 0), P = (1/4, 1/4, 1/4), N = (0, 1/2, 0), Z = (1/2, 1/2, −1/2), where the coordinates are represented in terms of basic vectors of the reciprocal lattice of the body-centered tetragonal lattice.

Acknowledge

We thank Toshiharu Chono, Tatsuro Aikawa, Shota Hayakawa, Hiroki Hanate, Shoya Kawano, Takumi Hasegawa, Tomoya Horide, Koji Miyazaki, Kazuyuki Matsuhira, Yoshihiko Okamoto, Koshi Takenaka, Takahiro Misawa, Yoshihide Yoshimoto, and Shinji Tsuneyuki for helpful discussions. We acknowledge the financial support of JSPS Kakenhi Grant JP19K03673, JP22H01183, and JP23H01126. A part of the computation was done at Supercomputer Center, Institute for Solid State Physics, University of Tokyo.

References

[1] Kazuma Nakamura et al. RESPACK: An *ab initio* tool for derivation of effective low-energy model of material. *Computer Physics Communications*, 261:107781, 2021.

[2] Mark S. Hybertsen and Steven G. Louie. *Ab initio* static dielectric matrices from the

density-functional approach. I: formulation and application to semiconductors and insulators. *Phys. Rev. B*, 35:5585–5601, Apr 1987.

[3] Claudia Ambrosch-Draxl and Jorge O. Sofo. Linear optical properties of solids within the full-potential linearized augmented planewave method. *Computer Physics Communications*, 175(1):1–14, 2006.

[4] Andrea Marini, Giovanni Onida, and Rodolfo Del Sole. Plane-wave dft-lda calculation of the electronic structure and absorption spectrum of copper. *Phys. Rev. B*, 64:195125, Oct 2001.

[5] Paolo Giannozzi et al. Quantum espresso: a modular and open-source software project for quantum simulations of materials. *Journal of Physics: Condensed Matter*, 21(39):395502 (19pp), 2009.

[6] Paolo Giannozzi et al. Advanced capabilities for materials modelling with quantum espresso. *Journal of Physics: Condensed Matter*, 29(46):465901, 2017.

[7] Shota Hayakawa et al. *Ab initio* calculation for electronic structure and optical property of tungsten carbide in a TiCN-based cermet for solar thermal applications. *Scientific Reports*, 13(1):9407, 2023.

[8] Kazuma Nakamura, Yoshiro Nohara, Yoshihide Yosimoto, and Yusuke Nomura. Ab initio GW plus cumulant calculation for isolated band systems: Application to organic conductor $(TMTSF)_2PF_6$ and transition-metal oxide $SrVO_3$. *Phys. Rev. B*, 93:085124, Feb 2016.

[9] Maxime Charlebois et al. *Ab initio* derivation of low-energy hamiltonians for systems with strong spin-orbit interaction: Application to $Ca_5Ir_3O_{12}$. *Phys. Rev. B*, 104:075153, Aug 2021.

[10] Makoto Wakeshima, Nobuyuki Taira, Yukio Hinatsu, and Yoshinobu Ishii. Electrical and magnetic properties of pseudo-one-dimensional calcium iridium oxide $Ca_5Ir_3O_{12}$. *Solid State Communications*, 125(6):311 – 315, 2003.

[11] Kazuyuki Matsuhira et al. Nonlinear conductivity of geometrically frustrated iridate $Ca_5Ir_3O_{12}$. *Journal of the Physical Society of Japan*, 87(1):013703, 2018.

[12] Hiroki Hanate et al. Insulating nature of iridium oxide $Ca_5Ir_3O_{12}$ probed by synchrotron-radiation-based infrared spectroscopy. *Journal of the Physical Society of Japan*, 92(6):064705, 2023.

[13] Hiroki Hanate et al. First observation of superlattice reflections in the hidden order at 105 k of spin–orbit coupled iridium oxide $Ca_5Ir_3O_{12}$. *Journal of the Physical Society of Japan*, 90(6):063702, 2021.

[14] Takumi Inohara, Yoshihiko Okamoto, Youichi Yamakawa, Ai Yamakage, and Koshi Takenaka. Large thermoelectric power factor at low temperatures in one-dimensional telluride Ta_4SiTe_4. *Applied Physics Letters*, 110(18):183901, 05 2017.

[15] Fumiya Matsunaga et al. Anisotropic optical conductivity accompanied by a small energy gap in the one-dimensional thermoelectric telluride Ta_4SiTe_4. *Phys. Rev. B*, 109:L161105, Apr 2024.

[16] Jun Yamauchi, Masaru Tsukada, Satoshi Watanabe, and Osamu Sugino. First-principles study on energetics of *c*-BN(001) reconstructed surfaces. *Phys. Rev. B*, 54:5586–5603, Aug 1996.

[17] Takahiro Misawa and otherso. mVMC: open-source software for many-variable variational monte carlo method. *Computer Physics Communications*, 235:447–462, 2019.

[18] Mitsuaki Kawamura et al. Quantum lattice model solver HPhi. *Computer Physics Communications*, 217:180–192, 2017.

[19] Tatsuro Aikawa, Tomoya Horide, and Kazuma Nakamura. *Ab initio* wannier analysis for cuprate la_2cuo_4 with bending strain. In *PROCEEDINGS OF 11th SYMPOSIUM ON APPLIED ENGINEERING AND SCIENCES 2023*.

[20] Hirofumi Sakakibara, Hidetomo Usui, Kazuhiko Kuroki, Ryotaro Arita, and Hideo Aoki. Two-orbital model explains the higher transition temperature of the single-layer Hg-cuprate superconductor compared to that of the La-cuprate superconductor. *Phys. Rev. Lett.*, 105:057003, Jul 2010.